

CrossMark  
click for updatesCite this: *J. Mater. Chem. A*, 2016, 4, 8803

# Hollow porous nanoparticles with Pt skin on a Ag–Pt alloy structure as a highly active electrocatalyst for the oxygen reduction reaction†

Tao Fu,<sup>a</sup> Jun Fang,<sup>\*b</sup> Chunsheng Wang<sup>c</sup> and Jinbao Zhao<sup>\*ad</sup>

Aiming to reduce the dosage of the noble metal Pt and improve the catalytic activity of the catalyst in fuel cells, hollow porous Ag–Pt alloy nanoparticles with Pt coating are prepared via a facile controlled galvanic replacement reaction. Ag is used as the substrate to build a hollow porous structure and alloyed with Pt to minimize the tensile effect of the Ag on the deposited Pt skin which would significantly lower the catalytic performance of the Ag–Pt bimetallic catalyst. This hollow porous Ag/Pt bimetallic catalyst exhibits a long catalytic durability and a mass activity of 0.438 A mg<sub>Pt</sub><sup>−1</sup> at 0.9 V (vs. RHE) towards the oxygen reduction reaction (ORR), which is ca. 3 times higher than that of the commercial Pt/C catalyst. The significant enhancement over the state-of-the-art Pt catalysts can be attributed to (1) the high surface area of the nanoparticles, (2) the more suitable d-band center of the Pt skin deposited on the Ag–Pt alloy substrate, and (3) the high thermal stability of the Ag–Pt alloy. Therefore, this work provides a new strategy for designing high-performance catalysts with low cost. In addition, the synthetic chemistry involved can possibly be extended for fabricating versatile catalysts with a similar structure.

Received 15th March 2016

Accepted 9th May 2016

DOI: 10.1039/c6ta02202b

www.rsc.org/MaterialsA

## Introduction

Fuel cells, as new energy conversion devices, exhibit great potential in solving energy crisis and environmental pollution, owing to their high energy density, desirable energy conversion efficiency and green conversion products.<sup>1,2</sup> In fuel cells, electrocatalysts are one of the most critical components for electrochemical performance. Until now, the platinum-based materials are still the most effective electrocatalysts in proton exchange membrane fuel cells.<sup>3–5</sup> Due to the high cost of Pt metal, the Pt load should be further reduced by significantly enhancing the mass catalytic activity and durability of the Pt catalysts.<sup>6–9</sup>

Extensive research studies have been conducted to develop highly catalytically active Pt catalysts. One of the most successful

technologies is to use metal–Pt bimetallic catalysts with a hollow structure or core–shell structure.<sup>10–12</sup> In comparison with solid Pt catalysts, Pt-based catalysts with a hollow structure or core–shell structure possess higher utilization of Pt atoms,<sup>13</sup> and the different elemental compositions and atomic arrangements can change the electronic structure of Pt, enhancing the Pt catalytic activity.<sup>14</sup> Ag is a cheap noble metal and has the lattice constant close to that of Pt, which could facilitate the growth of Pt on Ag. In addition, Ag–Pt alloy catalysts also have high thermodynamic stability, as calculated by Ramirez-Caballero *et al.* using density functional theory (DFT) calculations.<sup>15</sup> These unique properties of Ag–Pt bimetallic catalysts make the Ag–Pt catalysts very promising for catalytic applications.<sup>16–18</sup> However, the Ag sites on Ag–Pt alloys are non-reactive for the adsorption of chemisorbed oxygen, which would reduce the overall catalytic activity toward the oxygen reduction reaction (ORR) of Ag–Pt alloy catalysts.<sup>19</sup> Therefore, core–shell Ag@Pt catalysts should be better than Ag–Pt alloy catalysts. But the tensile effect of the Ag substrate on the Pt shell in core–shell Ag@Pt catalysts induced by the lattice mismatch of the two metals also reduces the catalytic activity of the Pt shell for the ORR because the d-band center of the Pt shell shifts upward.<sup>20–22</sup> Pt with a higher d-band center would strongly bind oxygenated intermediates in the ORR process, hindering the subsequent ORR step, and thus lowering the catalytic activity toward the ORR.<sup>23–25</sup> To reduce the tension of the Pt shell in Ag@Pt catalysts, Yang and co-workers alloyed the Ag core with Pd to form AgPd@Pt nanoparticles. The Pd component in the AgPd core could significantly reduce the tensile effect of the Ag core on the Pt shell layers and hence the Pt shell of AgPd@Pt

<sup>a</sup>State Key Lab of Physical Chemistry of Solid Surfaces, Department of Chemistry, Collaborative Innovation Center of Chemistry for Energy Materials, College of Chemistry and Chemical Engineering, Xiamen University, Xiamen, 361005, P. R. China. E-mail: jbzha@xmu.edu.cn

<sup>b</sup>Department of Chemical & Biochemical Engineering, College of Chemistry and Chemical Engineering, Xiamen University, Xiamen, 361005, P. R. China. E-mail: jfang@xmu.edu.cn

<sup>c</sup>Department of Chemical and Biomolecular Engineering, University of Maryland, College Park, MD 20740, USA

<sup>d</sup>School of Energy Research, Xiamen University, Xiamen, 361005, P. R. China

† Electronic supplementary information (ESI) available: TEM images of Ag nanoparticles, EDS spectra, XPS survey spectrum, high-resolution Ag 3d spectra, XRD patterns, SAED patterns and the UV-Vis absorption spectrum of HP-Ag/Pt, Ag@Pt, aged Ag@Pt and Pt/C, TEM images of the HP-Ag/Pt on VC-72R and Ag@Pt on VC-72R, tables with summarized information. See DOI: 10.1039/c6ta02202b

exhibited significantly higher ORR activity and durability.<sup>26</sup> The minimization of the Ag nanoparticle size to <3 nm and reducing the Ag content to <25% can also reduce the tension of Pt, which also exhibited better ORR activity and durability.<sup>27</sup> Therefore, the negative influence of the Ag core/substrate on the Pt shell layers could be minimized or eliminated by alloying the Ag core/substrate with other metals or reducing the atomic ratio of Ag to Pt.

Different from reported methodologies, we for the first time designed a unique Pt thin shell coated on hollow porous Ag–Pt alloy structures to reduce the tension of the Pt shell. The hollow porous morphology brought higher Pt utilization, and the small Ag–Pt alloy thickness and low Ag content (*ca.* 30%) significantly reduced the tension on the Pt skin; thus, the Pt-on-Ag/Pt structure would exhibit a largely enhanced catalytic performance.

We synthesized hollow porous Ag–Pt@Pt nanoparticles with Pt skin coated on Ag–Pt alloy structures (HP-Ag/Pt) using a facile and environmentally friendly one-pot method,<sup>28</sup> and investigated their catalytic activity for the ORR. For comparison, solid core–shell Ag@Pt nanoparticles were also prepared using the same method by simply adjusting the addition amount of reducing agent. The hollow porous Ag/Pt nanoparticles exhibited excellent ORR catalytic activity and better durability as compared to core–shell Ag@Pt nanoparticles and the commercial Pt/C catalyst.

## Experimental

### Materials

We bought silver nitrate ( $\text{AgNO}_3$ , 99.8%) and sodium borohydride ( $\text{NaBH}_4$ , 98%) from Aladdin Industrial Co. Ltd (Shanghai, China). Perchloric acid ( $\text{HClO}_4$ , analytical grade), polyvinylpyrrolidone (PVP, K-30), ascorbic acid (analytical grade), hydrogen peroxide ( $\text{H}_2\text{O}_2$ , 30 wt%) and trisodium citrate dehydrate (sodium citrate, analytical grade) were purchased from Sinopharm Chemical Reagent Co. Ltd (Shanghai, China), and potassium tetrachloroplatinate ( $\text{K}_2\text{PtCl}_4$ , 99.95%) was obtained from J&K Scientific Ltd (Beijing, China). Commercial 40 wt% Pt/C (Johnson Matthey, HiSPEC<sup>TM</sup> 4000), Vulcan XC-72R carbon support (Cobalt Corp.) and Nafion ionomer (5 wt%) were supplied by Shanghai Hesen Electrical Ltd (Shanghai, China).

Unless otherwise stated, other reagents were of analytical grade and all chemicals were used as received without further purification.

### Preparation of Ag nanoparticles

~10 nm Ag nanoparticles were prepared from the  $\text{NaBH}_4$  reduction of  $\text{AgNO}_3$ . In a typical process,  $\text{AgNO}_3$  (6.0 mg) and sodium citrate (14.0 mg) were added to 20 mL of deionized water in a round bottom flask and vigorously stirred at room temperature. Then, an aqueous  $\text{NaBH}_4$  solution (0.6 mL, 100 mM) was added dropwise. The color of the solution would turn from colorless to pale brown immediately. The solution was constantly stirred for 24 h to completely decompose the residual  $\text{NaBH}_4$  and then the Ag nanoparticles dispersed in the aqueous solution were obtained and used in the subsequent process directly.

### Preparation of hollow porous Ag–Pt@Pt nanoparticles (HP-Ag/Pt)

A one-pot approach was used to synthesize HP-Ag/Pt. In brief, ascorbic acid (16.0 mg), PVP (18.0 mg),  $\text{K}_2\text{PtCl}_4$  (9.0 mg) and the previously synthesized Ag nanoparticle dispersion were mixed and heated to 85 °C under stirring in a flask. The formation of the product was indicated by the color change of the mixture from brown to black at about 80 °C. And another 5.6 mg  $\text{K}_2\text{PtCl}_4$  (the total amount of  $\text{K}_2\text{PtCl}_4$  is 14.6 mg, so the molar ratio of Ag and Pt precursors was 50 : 50) was added into the flask when the reaction temperature reached 85 °C and kept at 85 °C for 1 h. After the reaction, the HP-Ag/Pt nanoparticles were purified by precipitation with deionized water twice, and re-dispersed in deionized water (5 mL). If the PVP was not fully rinsed, 1.0 mL 30 wt%  $\text{H}_2\text{O}_2$  could be added into the dispersion of the product and then the samples were collected by precipitation after 12 h.

### Preparation of core–shell Ag@Pt nanoparticles (Ag@Pt)

To synthesize Ag@Pt, more reducing agent is needed to avoid galvanic replacement between Ag and  $\text{PtCl}_4^{2-}$ . So in this approach, the addition of ascorbic acid was doubled. Ascorbic acid (32.0 mg) and PVP (18.0 mg) and the previously synthesized Ag nanoparticle dispersion were mixed and heated to 85 °C under stirring; then,  $\text{K}_2\text{PtCl}_4$  (14.6 mg, the Ag and Pt precursor molar ratio was 50 : 50) was added. The rapid formation of the product was indicated by the color change of the mixture from brown to dark brown which was visually nearly black. The solution was kept at 85 °C for 1 h and then the Ag@Pt nanoparticles were purified by precipitation with deionized water twice, and re-dispersed in deionized water (5 mL). If the PVP was not fully rinsed, 1.0 mL 30 wt%  $\text{H}_2\text{O}_2$  could be added into the dispersion of the product and then the samples were collected by precipitation after 12 h.

### Characterization

The morphology of the products was characterized by transmission electron microscopy (TEM, JEOL JEM-1400 and FEI Tecnai G2 F30). The elemental composition of the nanoparticles was obtained using electron energy dispersive X-ray (EDX) analysis. The elemental contents (Ag and Pt) of the samples were detected by the inductively coupled plasma (NCS Testing Technology, Plasma1000) technique. The crystalline information of the products was examined by using an X-ray diffractometer (Rigaku, Mini Flex 600) using  $\text{Cu K}\alpha$  radiation at 34–90° and a scan rate of 1.0° min<sup>−1</sup>.

The electronic structure and surface contents were evaluated by X-ray photoelectron spectroscopy (PHI QUANTUM 2000) using Al  $\text{K}\alpha$  radiation. The binding energy was referenced to the C 1s spectrum at 284.6 eV. A UV/VIS/NIR spectrometer (HITA-CHI U-3900H) was used to obtain the ultraviolet visible (UV-Vis) spectra of the nanoparticles.

### Electrochemical measurements

Electrochemical measurements were carried out in a standard three-electrode cell connected to a CHI 730E dual channel electrochemical workstation (CH Instruments, Inc.). A leak-free

Ag/AgCl (saturated with KCl) electrode was used as the reference electrode and a graphite electrode was used as the counter electrode. All the potentials were measured against a reversible hydrogen electrode (RHE).

Before we prepared the working electrode, both HP-Ag/Pt and Ag@Pt were loaded on a Vulcan XC-72R carbon support according to the following process: the calculated amount of carbon support was dispersed in H<sub>2</sub>O (2 mL) and sonicated for 5 h before the addition of HP-Ag/Pt or Ag@Pt nanoparticles dispersed in H<sub>2</sub>O (1 mL). The Pt loading amount of nanoparticles was fixed at 40 wt% of the final product to be comparable to that of the commercial Pt/C (40 wt% Pt). The mixed dispersion was stirred for 24 h and then the HP-Ag/Pt on the carbon support (40 wt% Pt) or Ag@Pt on the carbon support (40 wt% Pt) was collected *via* centrifugation at 10 000 rpm for 20 min. The precipitate was washed twice with ethanol and dried at room temperature in a vacuum.

The catalyst ink was prepared by sonicating the electrocatalyst samples (1.5 mg mixture of HP-Ag/Pt on carbon, Ag@Pt on carbon or commercial Pt/C), ethanol (980  $\mu$ L), and Nafion solution (0.5 wt%; 20  $\mu$ L) for 3 h. Then, 5  $\mu$ L ink was dropped onto a freshly polished glassy carbon of a rotating disk working electrode (RDE, 5.61 mm in diameter and 0.247 cm<sup>2</sup> in surface area, PINE Instrument Co. Ltd) and left to dry. The Pt loading on all working electrodes is 3  $\mu$ g (12.15  $\mu$ g cm<sup>-2</sup>).

Cyclic voltammetry (CV) plots and CO stripping voltammetry plots of different samples were used to evaluate the electrochemically active surface areas (ECSAs). The CV curves were recorded in N<sub>2</sub>-saturated 0.1 M HClO<sub>4</sub> at room temperature with a scan rate of 50 mV s<sup>-1</sup>. To obtain the CO stripping curves, CO (>99.9%, Xinhang) was introduced into 0.1 M HClO<sub>4</sub> for 20 min, meanwhile the working electrode was held at 0.05 V. Then the solution was purged with N<sub>2</sub> for 25 min to remove the dissolved CO, and then CO stripping curves were recorded between -0.05 and 1.30 V with a scan rate of 50 mV s<sup>-1</sup>. The electrocatalytic activity for the ORR was evaluated using linear scanning voltammetry (LSV) in O<sub>2</sub>-saturated 0.1 M HClO<sub>4</sub> solution at a scan rate of 10 mV s<sup>-1</sup> and a rotating speed of 1600 rpm. The durability of the electrocatalyst toward the ORR was evaluated using the accelerated durability test (ADT) and chronoamperometric plots; ADT was carried out by potential cycling between 0.60 and 1.00 V for 15 000 cycles in an O<sub>2</sub>-saturated 0.1 M HClO<sub>4</sub> solution at a scan rate of 50 mV s<sup>-1</sup>, and chronoamperometric plots were recorded in an O<sub>2</sub>-saturated 0.1 M HClO<sub>4</sub> solution at a rotating speed of 1600 rpm.

Unless otherwise stated, all of the measurements were carried out at room temperature.

## Results and discussion

### Synthesis of the hollow porous Ag-Pt@Pt (HP-Ag/Pt) and core-shell Ag@Pt nanoparticles

The synthesis process of the hollow porous Ag-Pt@Pt (HP-Ag/Pt) and core-shell Ag@Pt nanoparticles is schematically shown in Scheme 1.

As shown in Scheme 1, when PtCl<sub>4</sub><sup>2-</sup> is introduced into an aqueous suspension of Ag nanoparticles with a reducing agent

like ascorbic acid (AA), PtCl<sub>4</sub><sup>2-</sup> would be reduced to Pt atoms through two competing parallel reactions involving AA or Ag. The reaction rates of these two competing reactions can be controlled by the concentration of AA and Ag under the same reaction conditions and would finally lead to different particle structures.<sup>29</sup>

When the concentration of AA is relatively low (*ca.* 4.5 mM, route A in Scheme 1), the AA reduction reaction and galvanic replacement reaction take place at the same time. A hollow porous Ag-alloyed-Pt shell can be built after adding the first 61.6% of PtCl<sub>4</sub><sup>2-</sup>. A part of the PtCl<sub>4</sub><sup>2-</sup> is reduced by AA into Pt atoms and epitaxially deposits on the surface of the Ag nanoparticles to form an incomplete thin Pt shell. In the meanwhile, PtCl<sub>4</sub><sup>2-</sup> also oxidizes Ag core nanoparticles through galvanic replacement. The Ag<sup>+</sup> produced by the galvanic replacement can also be reduced by AA and then deposited on the newly formed Pt layer, forming a porous Ag-Pt alloy shell on the Ag nanoparticles. The oxidized Ag atoms are dissolved into solution, generating a small hole on the Ag nanoparticles. This small hole serves as the primary site for continuous dissolution of Ag nanoparticles which would finally lead to an unclosed cavity. In this process, Ag nanoparticles function as sacrificial templates for the cavity in the product. Finally, the inner Ag nanoparticles are totally removed by the galvanic replacement and the hollow porous Ag-Pt alloy shells are left. In the following reduction of PtCl<sub>4</sub><sup>2-</sup>, the thin Pt film is coated on the hollow porous Ag-Pt shell; thus, a Pt skin on a hollow porous Ag-Pt alloy substrate structure is created.

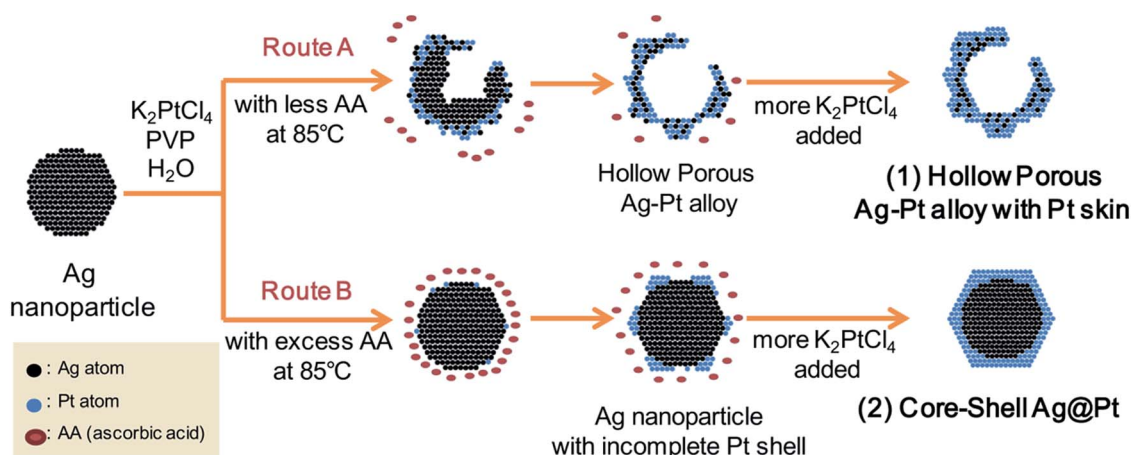
However, at a higher concentration (*ca.* 9.0 mM, route B in Scheme 1) of AA, the reduction reaction of AA would be faster than the galvanic replacement reaction. As a result, the galvanic replacement reaction is inhibited and the Pt atoms formed by the AA reduction reaction deposit on the Ag nanoparticles to generate a core-shell Ag@Pt structure.

### Characterization of the hollow porous Ag-Pt@Pt (HP-Ag/Pt) and core-shell Ag@Pt nanoparticles

The morphologies of the hollow porous Ag-Pt@Pt (HP-Ag/Pt) and core-shell Ag@Pt nanoparticles are characterized using TEM as presented in Fig. 1. HP-Ag/Pt nanoparticles exhibit a near spherical shape consisting of an irregular surface with holes and an internal cavity (highlighted by the red dashed line in Fig. 1c). The average particle size of HP-Ag/Pt nanoparticles is about 16.95 nm and the thickness of the shell is *ca.* 3.50 nm. The lattice fringes with a spacing of 0.227 nm in the surface layer of HP-Ag/Pt nanoparticles are associated well with the Pt {111} planes (0.2265 nm, JCPDS no. 04-0802), and the lattice fringes with a spacing of 0.231 nm underneath the surface Pt layer lay between Pt {111} planes and Ag {111} planes (0.2359 nm, JCPDS no. 04-0783), which can be assigned to the Ag-Pt alloy.

In contrast, the Ag@Pt nanoparticles are solid particles with a near hexagonal shape and the surface crystal facets are well-defined with a few lattice defect sites. The average diameter of Ag@Pt nanoparticles is 15.40 nm and the thickness of the Pt shell (indicated by the arrow in Fig. 1f) is 1.30–1.60 nm which





**Scheme 1** Synthetic schematic of (1) hollow porous nanoparticles with Pt skin on the Ag–Pt alloy structure and (2) core-shell Ag@Pt nanoparticles with Pt on the Ag structure via route A (major reaction:  $PtCl_4^{2-} + 2Ag \rightarrow Pt + 2Ag^+ + 4Cl^-$ ) and route B (major reaction:  $PtCl_4^{2-} + \text{ascorbic acid} \rightarrow Pt + 4Cl^-$ ), respectively.

contains 4 to 6 layers of Pt atoms. The lattice fringe spacing in the surface layer of Ag@Pt is 0.228 nm (close to Pt {111} planes) and in the interior of Ag@Pt is 0.236 nm (close to Ag {111} planes), showing the core-shell structure of Ag@Pt.

The structures of the synthesized two nanoparticles were further characterized using XRD and SAED. Fig. 2 shows the XRD patterns of Ag@Pt and HP-Ag/Pt. In the diffractions of Ag@Pt, the strong peak near  $2\theta = 38.6^\circ$  and the weaker peak at

$\sim 44.6^\circ$  correspond to the planes {111} and {200} of Ag. The peak near  $39.6^\circ$  and the weak one at  $\sim 45.7^\circ$  are distributed to the planes {111} and {200} of face-centered cubic (fcc) Pt. In the diffractions of HP-Ag/Pt, the diffraction peaks of Ag ({111} and {200}) disappear, and the  $2\theta$  value of the Pt {111} peak reduces from  $39.7^\circ$  to  $\sim 39.4^\circ$ , suggesting that Pt alloys with Ag atoms (the diameter of the Ag atom is 2.88 Å compared to 2.77 Å of the Pt atom) which increases the unit cell lattice parameter. The

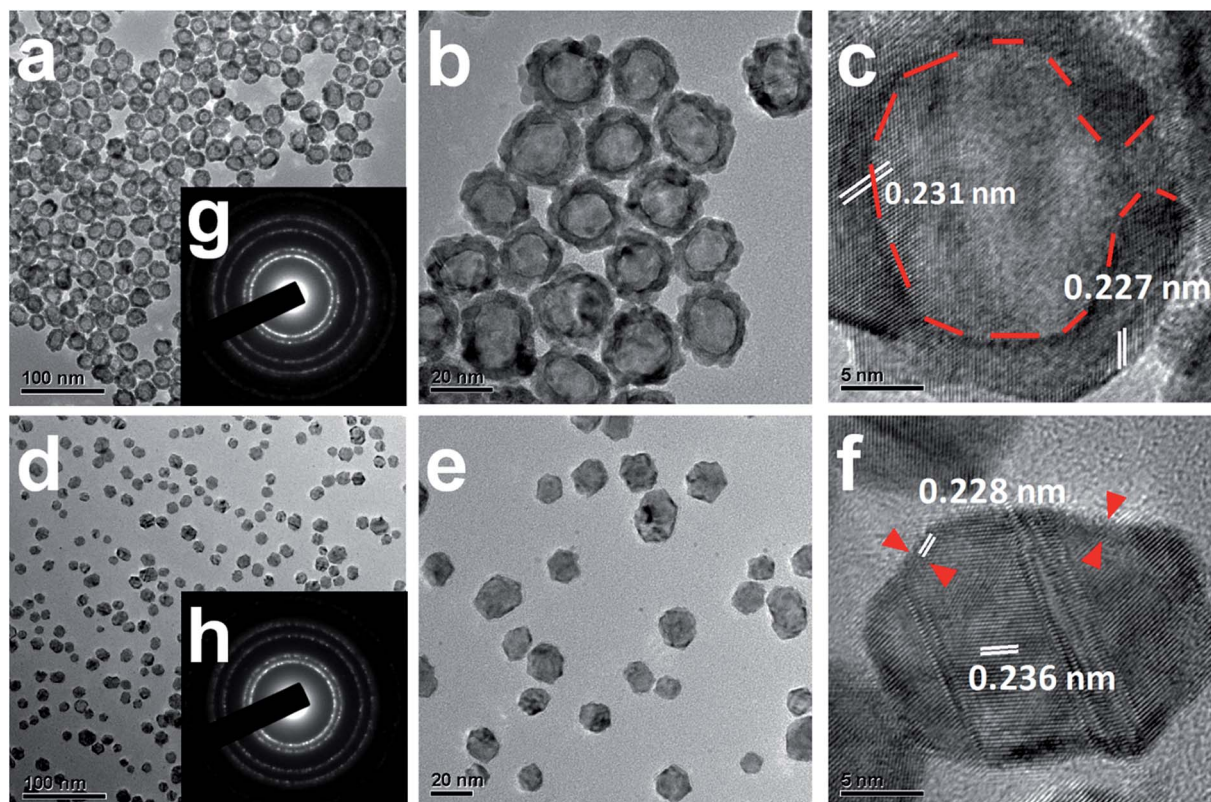


**Fig. 1** Representative TEM image of (a, b and c) the hollow porous Ag–Pt@Pt nanoparticles (HP-Ag/Pt) and (d, e and f) the core-shell Ag@Pt nanoparticles; insets (g and h) are the SAED patterns of the corresponding samples.

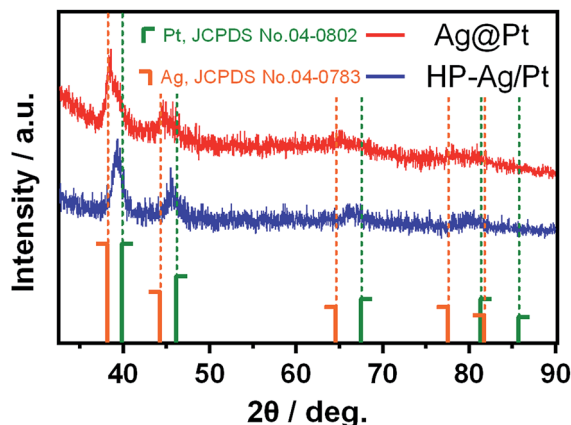


Fig. 2 XRD patterns of core-shell Ag@Pt and hollow porous Ag-Pt@Pt (HP-Ag/Pt) nanoparticles.

UV-Vis absorption spectrum shown in Fig. S1 (ESI<sup>†</sup>) demonstrates that the Ag@Pt sample has a typical absorption peak of Ag at 376 nm, which is absent in the HP-Ag/Pt sample. These results further confirm the existence of a Ag core in Ag@Pt nanoparticles, but a Ag-Pt alloy layer in HP-Ag/Pt nanoparticles.

The elemental contributions in the HP-Ag/Pt and Ag@Pt nanoparticles were analyzed using high angle annular dark-field scanning transmission electron microscopy (HAADF-STEM), together with energy dispersive X-ray (EDX). As shown in Fig. 3a–c, the hollow structure can be clearly observed in the elemental maps of Ag and Pt in HP-Ag/Pt. The average distribution diameter of the Ag element in a single nanoparticle is *ca.* 16.00 nm, which is larger than the diameter of template Ag nanoparticles (9.90 nm, Fig. S2<sup>†</sup>), indicating that Ag atoms diffuse out from the inner core and re-deposit on the newly formed Pt shell to form Ag-Pt alloys. The line profiles of Ag and Pt in HP-Ag/Pt (Fig. 3d) show that there is a 0.78 nm gap between the starting points of Pt and Ag elements (labeled by the dashed line). This gap is the thickness of the Pt skin of HP-Ag/Pt, corresponding to 2.4 layers of Pt atoms. The elemental mappings in Fig. 3e–g clearly show the solid Ag core and Pt shell. The line profile (Fig. 3h) of Ag takes a bell shape, which is characteristic of spherical solid particles, and the line profile of Pt shows a lower plain stage, indicating the existence of the Pt thin shell. The distance between the starting points of the Pt shape and Ag shape (labeled by the dashed line) is calculated to be *ca.* 1.36 nm, which is consistent with the thickness of the Pt shell acquired from HRTEM images of Ag@Pt previously.

The elemental composition of the HP-Ag/Pt and Ag@Pt nanoparticles was determined by EDS, ICP and XPS, and the results are shown in Table 1. The atomic ratios of Ag-to-Pt of the starting precursors are 50 : 50 and change in the final products. The HP-Ag/Pt sample exhibits a lower Ag-to-Pt atomic ratio which is caused by the galvanic replacement of the Ag core. The atomic ratio of Ag@Pt is close to that of the original precursors due to the block of the galvanic replacement between Ag and PtCl<sub>4</sub><sup>2-</sup>; therefore, there is hardly any Ag loss during the formation of Ag@Pt. EDS and ICP measurements lead to almost the same result; however, XPS analysis results of HP-Ag/Pt and

Ag@Pt nanoparticles show much lower Ag-to-Pt ratios of 23 : 77 and 31 : 69, respectively, indicating that HP-Ag/Pt and Ag@Pt nanoparticles are covered with Pt atoms on the surface. The comparison among the elemental results between XPS (surface analysis) and ICP or EDS (bulk analysis techniques) confirms the Pt skin on the Ag-Pt alloy structure of HP-Ag/Pt nanoparticles and the Pt shell on the Ag core structure of Ag@Pt nanoparticles.

### Electrocatalytic activities of hollow porous Ag-Pt@Pt (HP-Ag/Pt) and core-shell Ag@Pt towards the oxygen reduction reaction (ORR)

Both HP-Ag/Pt and Ag@Pt were loaded on a Vulcan XC-72R carbon support with a 40 wt% Pt loading amount for electrochemical measurements, which is confirmed by ICP (Table S1<sup>†</sup>). As shown by the representative TEM images in Fig. S5,† HP-Ag/Pt and Ag@Pt nanoparticles are well dispersed on the carbon support without changing the size distribution and the morphology of the nanoparticles. A commercial Pt/C catalyst (Johnson Matthey, HiSPEC™ 4000, 40 wt% Pt) was used as the baseline catalyst.

The CV curves (Fig. S6a<sup>†</sup>) of HP-Ag/Pt, Ag@Pt and Pt/C exhibit similar hydrogen adsorption/desorption peaks from 0.06 to 0.40 V, which are typical for the Pt surface in acidic electrolytes.<sup>30</sup> Neither of the HP-Ag/Pt or Ag@Pt catalysts shows the typical oxidation peak of pure Ag in acid solution at *ca.* 0.50 V (*vs.* RHE, in the forward sweep), which indicates the full surface coverage of Pt on the HP-Ag/Pt and core-shell Ag@Pt.

The CO stripping curves (Fig. 4a) of HP-Ag/Pt, Ag@Pt and Pt/C show that the peak of absorbed hydroxyl species (*E* *~* 0.65 V, *vs.* RHE, in the backward sweep) on the HP-Ag/Pt catalyst positively shifted *ca.* 15 mV compared to Pt/C catalysts. As the coverage of OH<sub>ad</sub> species on Pt blocks O<sub>2</sub> adsorption and inhibits the subsequent reaction,<sup>31,32</sup> the positive shift in the reduction potential of the surface reduction on the HP-Ag/Pt catalysts indicates the faster desorption of OH<sub>ad</sub> from the Pt surface and the weaker oxygen affinity of Pt.<sup>33,34</sup> Therefore, the catalytic activity of the HP-Ag/Pt catalyst toward the ORR should be better than that of commercial Pt/C.

Fig. 4b shows the electrochemically active surface areas (ECSA<sub>CO</sub>) of catalysts calculated from the ratio of the charge in the CO oxidation region after subtracting the base current of the subsequent CV curve from 420 μC cm<sup>-2</sup> for the specific charge of monolayer adsorption of CO.<sup>35</sup> The HP-Ag/Pt catalyst displays an ECSA<sub>CO</sub> of 94.1 m<sup>2</sup> g<sub>Pt</sub><sup>-1</sup>, which is higher than that of commercial Pt/C (74.5 m<sup>2</sup> g<sub>Pt</sub><sup>-1</sup>) and Ag@Pt catalysts (53.2 m<sup>2</sup> g<sub>Pt</sub><sup>-1</sup>). For HP-Ag/Pt, the hollow and porous structure possesses a high surface area and the irregular particle surface with curvature and minor prominence brings a lot of defects, edges, steps, and corner Pt atoms, which are suitable sites for catalysis due to their adjacent Pt arrangement;<sup>36,37</sup> so, there is a large amount of catalytically active sites on HP-Ag/Pt. In contrast, the larger particle sizes of the Ag@Pt catalyst (~15 nm, as compared to ~3 nm of Pt nanoparticles in the commercial Pt/C catalyst) lead to a smaller surface area and less catalytically active sites, which lower the ECSA<sub>CO</sub> of Ag@Pt. It is worth mentioning that



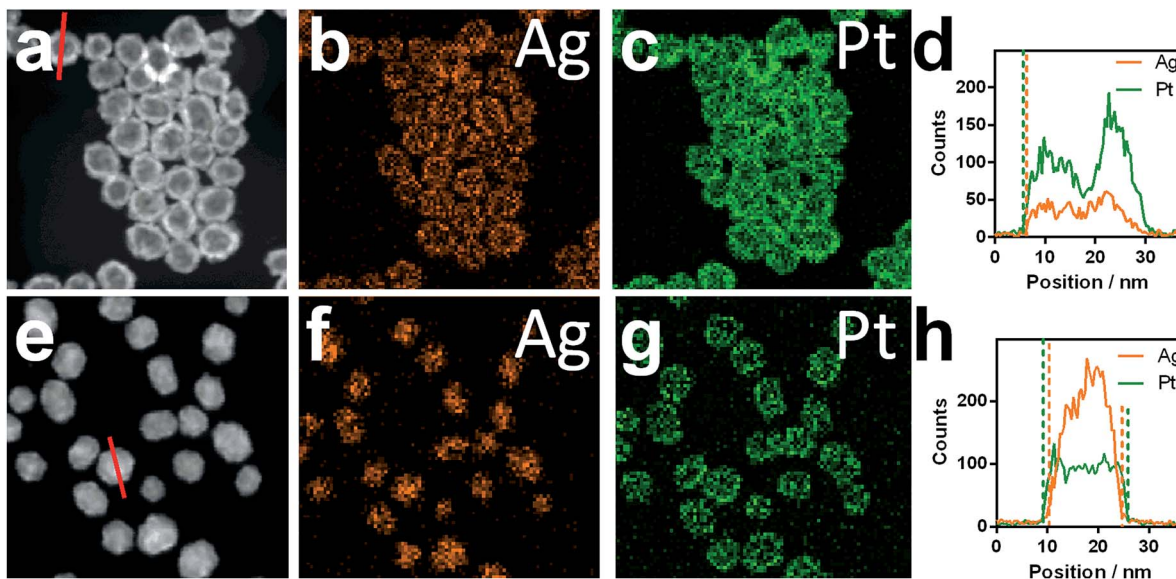


Fig. 3 HAADF-STEM images of (a, b and c) the hollow porous Ag–Pt@Pt (HP-Ag/Pt) nanoparticles and (e, f and g) the core–shell Ag@Pt nanoparticles with EDX elemental mapping. (d) and (h) are the corresponding STEM EDX line scans (red line) in (a) and (e), respectively.

Table 1 The atomic ratios of Ag-to-Pt measured by different methods

Sample	Atomic ratios <sup>a</sup>	Atomic ratios <sup>b</sup>	Atomic ratios <sup>c</sup>
HP-Ag/Pt	32 : 68	31 : 69	23 : 77
Ag@Pt	55 : 45	54 : 46	31 : 69

<sup>a</sup> Measured by EDS analysis (Fig. S3). <sup>b</sup> Measured by ICP analysis (Table S1). <sup>c</sup> Measured by XPS analysis (Fig. S4 and Table S2).

the ECSA<sub>CO</sub> of HP-Ag/Pt is much higher than its ECSA<sub>Hupd</sub> (calculated from hydrogen adsorption) which is attributed to the weakened hydrogen adsorption of the Pt skin on the AgPt alloy.<sup>38,39</sup>

The linear scanning voltammetry curves (LSV, Fig. 4c) were used to compare the electrocatalytic activities toward the oxygen reduction reaction (ORR) of HP-Ag/Pt, Ag@Pt, and Pt/C catalysts. The half-wave potentials are 900 mV for HP-Ag/Pt, 836 mV for Ag@Pt, and 856 mV for commercial Pt/C. The half-wave potential of HP-Ag/Pt is *ca.* 44 mV more positive than that of commercial Pt/C, suggesting a significant enhancement in ORR catalytic activity. And the half-wave potential of Ag@Pt is *ca.* 20 mV smaller than that of commercial Pt/C, which means that the ORR catalytic activity of the Ag@Pt catalyst is limited.

To compare the ORR activity of the catalysts, the kinetic current densities (*i<sub>k</sub>*) of these catalysts were calculated by applying the Koutecký–Levich equation and normalized with respect to both ECSAs and the loading amount of metal Pt (calculated ORR activities are summarized in Table S3†). The mass activities of the three catalysts at 0.90 V (room temperature) are shown in Fig. 4d. The mass activities of HP-Ag/Pt, Ag@Pt and commercial Pt/C at 0.90 V (vs. RHE) are 0.438 A mg<sub>Pt</sub><sup>−1</sup>, 0.073 A mg<sub>Pt</sub><sup>−1</sup> and 0.148 A mg<sub>Pt</sub><sup>−1</sup>, respectively. The HP-Ag/Pt exhibits the highest mass activity which is 3 times

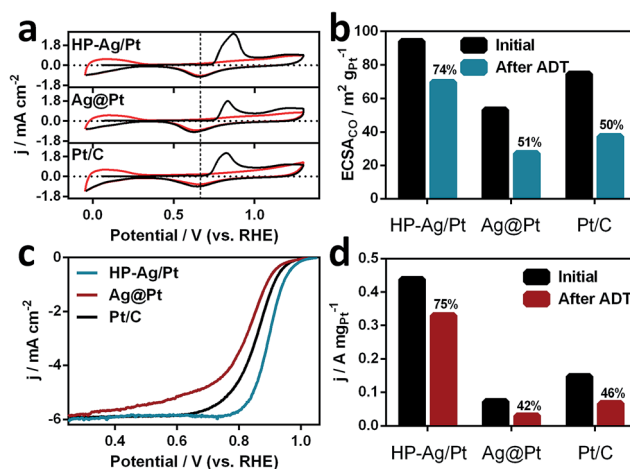


Fig. 4 The nanoparticles are loaded on an XC-72R and the Pt loading for all three samples is 40 wt%. (a) CO stripping voltammograms of HP-Ag/Pt, Ag@Pt and Pt/C in 0.1 M HClO<sub>4</sub> at room temperature and a scan rate of 50 mV s<sup>−1</sup>. (b) The electrochemical surface area (calculated from CO stripping) before and after the accelerated durability test (ADT), normalized by Pt mass. (c) Linear scan voltammograms in 0.1 M HClO<sub>4</sub> (RT) saturated with O<sub>2</sub> at a scan rate of 10 mV s<sup>−1</sup> and at a rotating speed of 1600 rpm. (d) The comparison of initial kinetic mass activities of the ORR at 0.90 V (vs. RHE) and after the accelerated durability test, normalized by Pt mass.

higher than that of the commercial Pt/C. Considering that this result is obtained at room temperature, this value is very close to the U.S Department of Energy (DOE) 2017 target, a mass activity of 0.44 A mg<sub>Pt</sub><sup>−1</sup> for Pt at 0.90 V at 80 °C under IR-free conditions. Furthermore, our HP-Ag/Pt catalyst exhibits one of the highest ORR catalytic activities (Table S4†) among the representative Ag–Pt catalysts reported in the literature reported to date.

The durability of the catalysts is examined using the accelerated durability test (ADT). Fig. 5 shows comparisons of CV curves and polarization curves for the ORR of HP-Ag/Pt, Ag@Pt and commercial Pt/C catalysts before and after the ADT. The CO stripping curves (Fig. S6†) show a loss of 26.0% in  $\text{ECSA}_{\text{CO}}$  for the HP-Ag/Pt catalyst, 49.1% for the Ag@Pt catalyst and 50.1% for the commercial Pt/C catalyst (the loss of  $\text{ECSA}_{\text{CO}}$  and  $\text{ECSA}_{\text{Hupd}}$  is summarized in Table S5†). The polarization curves after the durability test show that the cycling procedures have no obvious influence on the diffusion-limited current for all three catalysts. As shown in Fig. 4d, the mass activities of HP-Ag/Pt, Ag@Pt and commercial Pt/C catalysts at 0.90 V (vs. RHE) decreased to 0.330, 0.030 and 0.067  $\text{A mg}_{\text{Pt}}^{-1}$ , falling to 75.3%, 41.5% and 45.5%, respectively. These results reveal that the stability of the HP-Ag/Pt catalyst is also the best among the three catalysts and it is worth mentioning that the mass activity of the cycled HP-Ag/Pt catalyst is still *ca.* 2.2 times the mass activity of the fresh commercial Pt/C catalyst.

Furthermore, chronoamperometry of HP-Ag/Pt, Ag@Pt and commercial Pt/C at 0.90 V in  $\text{O}_2$ -saturated 0.1 M  $\text{HClO}_4$  is used to test the activity loss of catalysts in continuous ORR catalysis. Fig. 5d shows that the ORR current density of Ag@Pt and commercial Pt/C decreases to 11.8% of the original value after 20 min. In contrast, the activity conservation rate of HP-Ag/Pt is much higher (20.25%). The above results indicate that the HP-Ag/Pt nanoparticles possess higher stability than core-shell Ag@Pt and commercial Pt/C. According to the DFT calculation by Ramirez-Caballero *et al.*, there is a charge transfer between Ag and Pt due to their different radii, surface energy and cohesive energy, which would stabilize the Ag-Pt alloy structure under ORR catalyzing conditions.<sup>15</sup> The TEM images of cycled HP-Ag/Pt are shown in Fig. 6; the hollow porous structure of HP-Ag/Pt remains due to the high stability of the inner Ag-Pt alloy shell. And the surface of the nanoparticles becomes more irregular, which may be attributed to the dissolution of surface

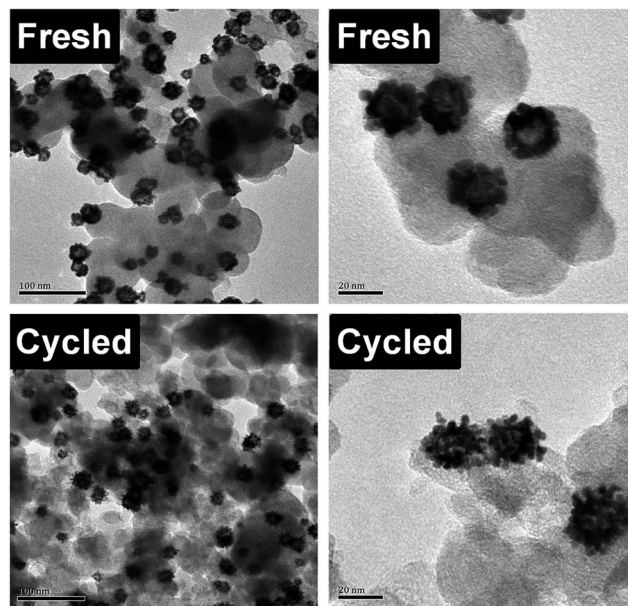


Fig. 6 The TEM images of fresh and cycled HP-Ag/Pt loaded on the XC-72R carbon support.

Pt atoms from the porous particles and the re-nucleation of Pt. In the case of Ag@Pt, the XPS and TEM measurements of cycled Ag@Pt (Fig. S7†) show that the Pt ratio of Ag@Pt is reduced after the ADT and the surface Pt layer atoms are dissolved or damaged during the ADT; therefore, the inner Pt layer becomes the new surface layer. The new surface Pt layer is more close to the Ag core, so it suffers more tensile effect and hence its ORR activity is lower, which degrades the performance of Ag@Pt after the ADT.

The HP-Ag/Pt catalyst shows a remarkable enhancement in the ORR catalytic performance while the Ag@Pt catalyst shows a feeble ORR catalytic activity. This disparity in the ORR catalytic performance can be attributed to the different morphological structures and electronic structures of these two catalysts. First, the catalyst with higher Pt utilization may possess better catalytic activity. The hollow porous structure of the HP-Ag/Pt catalyst leads to a higher ECSA which means that there are more catalytically active sites for the ORR on the HP-Ag/Pt nanoparticles. In contrast, the solid core-shell structure of the Ag@Pt catalyst has a smaller surface area which leads to a lower ECSA; therefore, the number of catalytically active sites on Ag@Pt nanoparticles is less than that on HP-Ag/Pt and Pt/C catalysts. Second, the electronic structure of the Pt surface in catalysts is also important to the catalytic activity of catalysts. A good Pt-based catalyst for the ORR should have a suitable d-band center to facilitate both the cleavage of O-O bonds and the formation of O-H bonds steps in the common ORR process.<sup>40</sup> The Pt surface with a higher d-band center would bind oxygenated intermediates in the ORR process too strongly and therefore hinder the bond-making step,<sup>41</sup> which leads to a lower catalytic activity for the ORR.<sup>42,43</sup> Since the lattice parameter of Ag (0.4090 nm) is larger than that of Pt (0.3923 nm), there would be a tensile effect exerted on the Pt skin by the Ag core/substrate

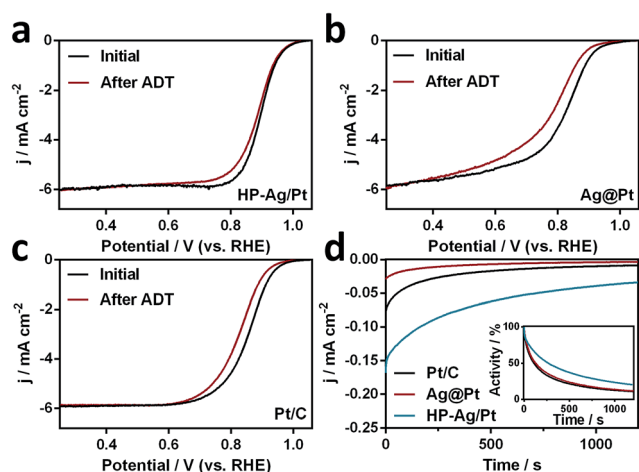


Fig. 5 The ORR polarization curves of the catalysts in  $\text{O}_2$ -saturated 0.1 M  $\text{HClO}_4$  before and after 15 000 cycles of durability test: (a) HP-Ag/Pt, (b) Ag@Pt and (c) commercial Pt/C catalysts. (d) Chronoamperograms of HP-Ag/Pt, Ag@Pt and Pt/C at 0.90 V (vs. RHE) in  $\text{O}_2$ -saturated 0.1 M  $\text{HClO}_4$  at room temperature and a rotating speed of 1600 rpm. The inset is the activity conservation rate of the three catalysts.

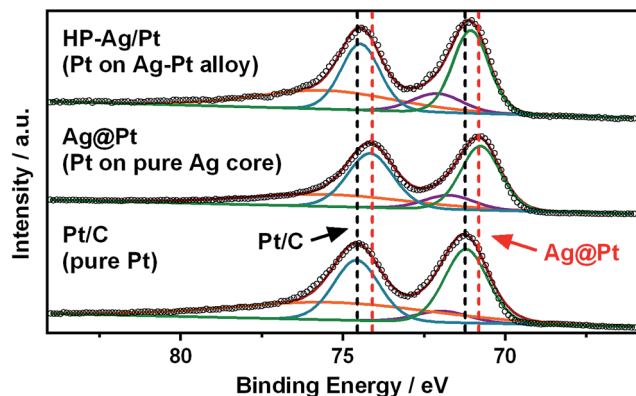


Fig. 7 High-resolution Pt 4f spectra of hollow porous Ag–Pt@Pt (HP-Ag/Pt), core–shell Ag@Pt nanoparticles and Pt/C.

underneath. The tensile effect would change the width of the d-band and the energy of its center without changing the degree of d-band filling. The average coordination number of the Pt atom decreases, which decreases the overlap of d orbitals and consequently narrows the d band. Then the d-band center would move up to maintain the same degree of filling.<sup>44</sup> Finally, the tensile effect of the Ag core/substrate on the deposited Pt shell brings an upward shift of the d-band center of the Pt shell and decreases its ORR catalytic activity. XPS measurements are applied to analyze the tensile effect in the HP-Ag/Pt and Ag@Pt catalysts. Due to the upward shift of the d-band center of the Pt shell, the d-electrons become closer to the Fermi level and more unstable, which decreases the Pt XPS binding energies. Therefore, the tensile effect can be found in the Pt 4f XPS spectra, as shown in Fig. 7 (summarized in Table S6†).<sup>17</sup>

The Pt 4f XPS spectra of HP-Ag/Pt, Ag@Pt and Pt/C samples can be deconvoluted into two pairs of doublets. All three samples show similar Pt 4f spectra with a strong doublet at ~71.2 and ~74.5 eV which is characteristic of Pt, and the weaker doublet at ~71.9 and ~75.4 eV can be attributed to oxidized Pt, such as Pt(OH)<sub>2</sub> and PtO. The Pt binding energies of Ag@Pt shift negatively (~0.6 eV) as compared to those of commercial Pt/C, which is caused by the tensile effect. In contrast, the Pt binding energies of HP-Ag/Pt are very close to that of Pt/C, indicating that the tensile effect of the Ag substrate is minimized by alloying the Ag substrate with Pt atoms. Therefore, the d-band center of the Pt skin in HP-Ag/Pt would not move to a value that is high enough to hinder the bond-making step; moreover, the new d-band center may be able to balance the cleavage of O–O bonds and the formation of O–H bonds steps better and lead to the enhanced catalytic activity toward the ORR.

## Conclusions

Hollow porous Ag–Pt@Pt nanoparticles with enhanced ORR catalytic activity were prepared using controlled galvanic replacement between Ag nanoparticles and PtCl<sub>4</sub><sup>2-</sup> in aqueous solution. The structure of the Pt skin on hollow porous Ag–Pt alloy nanoparticles was confirmed by TEM, EDX and XPS methods. These Ag/Pt bimetallic nanoparticles exhibited

a superior mass activity of 0.438 A mg<sub>Pt</sub><sup>−1</sup> at 0.9 V (vs. RHE) toward the ORR, which was ca. 3 times higher than that of the commercial Pt/C catalyst and also possessed exceptional catalytic stability. And the mechanism behind the enhanced performance was investigated using electrochemical measurements and XPS analysis. The hollow porous structure could increase the utilization of Pt atoms, and the Pt component in the Ag–Pt substrate could minimize the tensile effect of Ag on the deposited Pt skin and move the d-band center of the Pt skin to a more suitable value, which finally led to a high performance Ag–Pt bimetallic catalyst. Considering the relatively large particle size of HP-Ag/Pt nanoparticles (16.95 nm compared to ca. 3 nm of the commercial Pt/C catalyst), the catalytic performance of HP-Ag/Pt nanoparticles could be further improved by decreasing their particle size and adjusting the Ag-to-Pt molar ratio which would enlarge the surface area and the Pt utilization percent of HP-Ag/Pt nanoparticles.

Above all, this original research work provides an effective way to build a hollow porous structure and hence decreases the Pt loading amount of Pt-based catalysts while improving their catalytic activity simultaneously, which may be helpful in the design and synthesis of novel high performance catalysts.

## Acknowledgements

We gratefully acknowledge the financial support by the High-Tech Research and Development Program of China (No. 2008AA05Z107), National Natural Science Foundation of China (No. 20876129, 21376195 and 21321062) and National Found for Fostering Talents of Basic Science (J1310024). We thank Yunyang Ling for the assistance in obtaining the UV-Vis spectra, Qiang Wang for the instruction in instrument and methods of ORR experiments and Panyang Ji for the assistance in experiments.

## Notes and references

- 1 Y. Bing, H. Liu, L. Zhang, D. Ghosh and J. Zhang, *Chem. Soc. Rev.*, 2010, **39**, 2184–2202.
- 2 Z. Chen, D. Higgins, A. Yu, L. Zhang and J. Zhang, *Energy Environ. Sci.*, 2011, **4**, 3167.
- 3 J. Wu and H. Yang, *Acc. Chem. Res.*, 2013, **46**, 1848–1857.
- 4 J. Chen, B. Lim, E. P. Lee and Y. Xia, *Nano Today*, 2009, **4**, 81–95.
- 5 N. S. Porter, H. Wu, Z. Quan and J. Fang, *Acc. Chem. Res.*, 2013, **46**, 1867–1877.
- 6 F. A. de Bruijn, V. A. T. Dam and G. J. M. Janssen, *Fuel Cells*, 2008, **8**, 3–22.
- 7 H. A. Gasteiger and N. M. Markovic, *Science*, 2009, **324**, 48–49.
- 8 J. Greeley, J. Rossmeisl, I. E. L. Stephens, I. Chorkendorff, A. S. Bondarenko, J. K. Nørskov, T. P. Johansson, H. A. Hansen and T. F. Jaramillo, *Nat. Chem.*, 2009, **1**, 552–556.
- 9 J. K. Nørskov, T. Bligaard, J. Rossmeisl and C. H. Christensen, *Nat. Chem.*, 2009, **1**, 37–46.



- 10 X. Xia, Y. Wang, A. Ruditskiy and Y. Xia, *Adv. Mater.*, 2013, **25**, 6313–6333.
- 11 R. Ghosh Chaudhuri and S. Paria, *Chem. Rev.*, 2012, **112**, 2373–2433.
- 12 L. Gan, C. Cui, S. Rudi and P. Strasser, *Top. Catal.*, 2013, **57**, 236–244.
- 13 C. J. Serpell, J. Cookson, D. Ozkaya and P. D. Beer, *Nat. Chem.*, 2011, **3**, 478–483.
- 14 X. Zhou, Y. Gan, J. Du, D. Tian, R. Zhang, C. Yang and Z. Dai, *J. Power Sources*, 2013, **232**, 310–322.
- 15 G. E. Ramirez-Caballero, Y. Ma, R. Callejas-Tovar and P. B. Balbuena, *Phys. Chem. Chem. Phys.*, 2010, **12**, 2209–2218.
- 16 C. Li and Y. Yamauchi, *Phys. Chem. Chem. Phys.*, 2013, **15**, 3490–3496.
- 17 H. Liu and J. Yang, *J. Mater. Chem. A*, 2014, **2**, 7075.
- 18 W. He, X. Wu, J. Liu, K. Zhang, W. Chu, L. Feng, X. Hu, W. Zhou and S. Xie, *Langmuir*, 2010, **26**, 4443–4448.
- 19 H. You, Z. Peng, J. Wu and H. Yang, *Chem. Commun.*, 2011, **47**, 12595–12597.
- 20 Z. Peng, J. Wu and H. Yang, *Chem. Mater.*, 2010, **23**, 1098–1106.
- 21 N. Deogratias, M. Ji, Y. Zhang, J. Liu, J. Zhang and H. Zhu, *Nano Res.*, 2014, **8**, 271–280.
- 22 H. Liu, F. Ye, Q. Yao, H. Cao, J. Xie, J. Y. Lee and J. Yang, *Sci. Rep.*, 2014, **4**, 3969.
- 23 T. Bligaard and J. K. Nørskov, *Electrochim. Acta*, 2007, **52**, 5512–5516.
- 24 V. R. Stamenkovic, B. S. Mun, M. Arenz, K. J. Mayrhofer, C. A. Lucas, G. Wang, P. N. Ross and N. M. Markovic, *Nat. Mater.*, 2007, **6**, 241–247.
- 25 V. R. Stamenkovic, B. Fowler, B. S. Mun, G. Wang, P. N. Ross, C. A. Lucas and N. M. Markovic, *Science*, 2007, **315**, 493–497.
- 26 J. Yang, J. Yang and J. Y. Ying, *ACS Nano*, 2012, **6**, 9373–9382.
- 27 J. Cao, M. Guo, J. Wu, J. Xu, W. Wang and Z. Chen, *J. Power Sources*, 2015, **277**, 155–160.
- 28 P. T. Anastas and M. M. Kirchhoff, *Acc. Chem. Res.*, 2002, **35**, 686–694.
- 29 Y. Yang, J. Liu, Z. W. Fu and D. Qin, *J. Am. Chem. Soc.*, 2014, **136**, 8153–8156.
- 30 S. Mukerjee, *J. Appl. Electrochem.*, 1990, **20**, 537–548.
- 31 J. X. Wang, J. Zhang and R. R. Adzic, *J. Phys. Chem. A*, 2007, **111**, 12702–12710.
- 32 N. M. Markovic, H. A. Gasteiger, B. N. Grgur and P. N. Ross, *J. Electroanal. Chem.*, 1999, **467**, 157–163.
- 33 C. Wang, M. Chi, D. Li, D. Strmcnik, D. van der Vliet, G. Wang, V. Komanicky, K. C. Chang, A. P. Paulikas, D. Tripkovic, J. Pearson, K. L. More, N. M. Markovic and V. R. Stamenkovic, *J. Am. Chem. Soc.*, 2011, **133**, 14396–14403.
- 34 K. J. Mayrhofer, B. B. Blizanac, M. Arenz, V. R. Stamenkovic, P. N. Ross and N. M. Markovic, *J. Phys. Chem. B*, 2005, **109**, 14433–14440.
- 35 O. A. Baturina, B. D. Gould, Y. Garsany and K. E. Swider-Lyons, *Electrochim. Acta*, 2010, **22**, 6676–6686.
- 36 S. W. Lee, S. Chen, W. Sheng, N. Yabuuchi, Y. Kim, T. Mitani, E. Vescovo and S. Yang, *J. Am. Chem. Soc.*, 2009, **131**, 15669–15677.
- 37 L. Liu, E. Pippel, R. Scholz and U. Gosele, *Nano Lett.*, 2009, **9**, 4352–4358.
- 38 S. Rudi, C. Cui, L. Gan and P. Strasser, *Electrocatalysis*, 2014, **5**, 408–418.
- 39 D. F. van der Vliet, C. Wang, D. Li, A. P. Paulikas, J. Greeley, R. B. Rankin, D. Strmcnik, D. Tripkovic, N. M. Markovic and V. R. Stamenkovic, *Angew. Chem.*, 2012, **51**, 3139–3142.
- 40 J. Zhang, M. B. Vukmirovic, K. Sasaki, A. U. Nilekar, M. Mavrikakis and R. R. Adzic, *J. Am. Chem. Soc.*, 2005, **127**, 12480–12481.
- 41 Y. Xu, A. V. Ruban and M. Mavrikakis, *J. Am. Chem. Soc.*, 2004, **126**, 4717–4725.
- 42 V. Stamenković, T. J. Schmidt, P. N. Ross and N. M. Marković, *J. Phys. Chem. B*, 2002, **106**, 11970–11979.
- 43 N. Markovic, *J. Electrochem. Soc.*, 1997, **144**, 1591.
- 44 J. Zhang, M. B. Vukmirovic, Y. Xu, M. Mavrikakis and R. R. Adzic, *Angew. Chem., Int. Ed.*, 2005, **44**, 2132–2135.